NJC

New Journal of Chemistry

A journal for new directions in chemistry

Accepted Manuscript

This article can be cited before page numbers have been issued, to do this please use: M. Farfán-Paredes, O. González-Antonio, D. E. Tahuilan-Anguiano, J. Peón, A. Ariza-Castolo, P. G. Lacroix, R. Santillan and N. Farfán, *New J. Chem.*, 2020, DOI: 10.1039/D0NJ02576C.

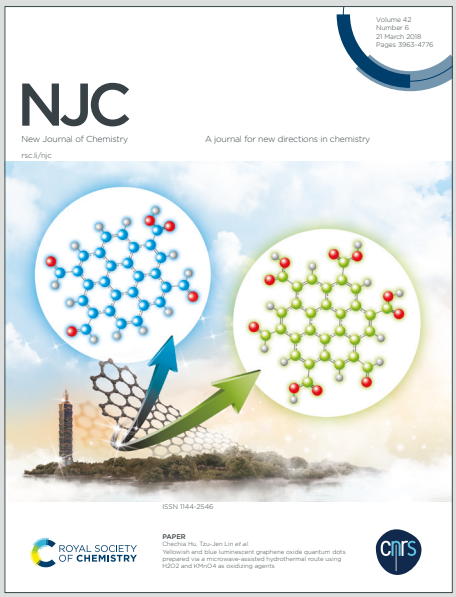

This is an Accepted Manuscript, which has been through the Royal Society of Chemistry peer review process and has been accepted for publication.

Accepted Manuscripts are published online shortly after acceptance, before technical editing, formatting and proof reading. Using this free service, authors can make their results available to the community, in citable form, before we publish the edited article. We will replace this Accepted Manuscript with the edited and formatted Advance Article as soon as it is available.

You can find more information about Accepted Manuscripts in the Information for Authors.

Please note that technical editing may introduce minor changes to the text and/or graphics, which may alter content. The journal's standard Terms & Conditions and the Ethical guidelines still apply. In no event shall the Royal Society of Chemistry be held responsible for any errors or omissions in this Accepted Manuscript or any consequences arising from the use of any information it contains.

View Article Online
DOI: 10.1039/D0NJ02576C

ARTICLE

Physicochemical and Computational Insight of ^{19}F NMR and Emission Properties of *meso*-(*o*-aryl)-BODIPYs

Received 00th January 20xx,
Accepted 00th January 20xx

DOI: 10.1039/x0xx00000x

Mónica Farfán-Paredes,[a] Oscar González-Antonio,[a] Diana E. Tahuilan-Anguiano,[a] Jorge Peón,[b] Armando Ariza,[c] Pascal G. Lacroix,[d] Rosa Santillan,[c] Norberto Farfán [a]*

A series of electronic and physicochemical parameters were explored to determine their effect on experimental spectroscopic and photophysical data. Through a systematic obtention of a series of *meso*-(*o*-aryl)-BODIPYs, ^{19}F NMR spectra were analyzed and their fluorescence quantum yields in several solvents were measured. Experimental values of ^{19}F chemical shift difference $\Delta\delta_F$ correlate well with σ-Hammett constants, which is indicative of the inductive nature of the functional groups on the fluorine atoms. A computational DFT exploration of rotational energy barriers, electrostatic potential maps, group electronegativity, charge partitions and hardness/softness, provided insight on how those traits can be directly related to the measured features. Expanded understanding of such characteristics provides design arguments and a structure-property relationship, which in a more advantageous way, would help to understand the properties of the synthesized molecules and of future attempts that are structurally related.

Introduction

The family of 4,4-difluoro-4-bora-3a,4a-diaza-s-indacene derivatives, also known as BODIPYs, are strongly UV-absorbing small molecules that emit relatively sharp fluorescence peaks. [1] These compounds are versatile dyes of considerable interest owing to their photochemical stability, synthetic versatility and good solubility in common organic solvents. Moreover, they show large extinction coefficients and tunable quantum yields.[2–5] For these properties, BODIPY-based dyes have been exploited as fluorescent probes,[6] molecular sensors,[7] semiconducting materials,[8–10] biological labelling agents,[11] viscosity probes[12] and photosensitizers in photodynamic therapy.[13] Another advantage is that it is possible to tune their spectroscopic and photophysical properties functionalizing adequately any position at the core including boron substituents.[14]

The BODIPY core has two pyrrole rings fused with a bridging carbon known as the 8 position or *meso* position and a BF_2 unit closing a third ring. The structure is co-planar with the electronic density distributed between three rings, while the two fluorine atoms are in a perpendicular plane. [15] The derivatives with *p*-substituted phenyl ring at *meso* position have freedom of movement and are considerably less fluorescent in comparison with the *ortho*-phenyl substituted which have restricted movement.[16] A wide variety of groups have been introduced at the *ortho* position of the *meso*-phenyl moiety in order to study their influence over the photophysical properties,[3,17] however, the influence of this *ortho*-substituents over fluorine atoms have rarely been studied.[18]

In this work, different substituents were introduced at the *ortho*-position of the *meso*-phenyl moiety in order to block freedom of rotation and study their influence over fluorine atoms by ^{19}F NMR, as well as its photophysical properties in four different solvents. Computational analyses for electrostatic interactions, hardness/softness and dipole moment were carried out and compared with experimental spectroscopic and photophysical results. Furthermore, the relationship between ^{19}F chemical shift difference ($\Delta\delta_F$) of the BODIPY derivatives with the group electronegativity and the σ-Hammett coefficients were investigated.

Results and Discussion

Synthesis and NMR characterization

BODIPYs **1-11** were synthesized using the sequence of reactions depicted in Scheme 1. BODIPYs **1-3** were prepared to compare with those that have *ortho*-substituents at the phenyl moiety. Additionally, a BODIPY with a bulky group (pyrene) **11** was also synthesized. All compounds were characterized by ^{1}H and ^{13}C,

[a] Facultad de Química, Departamento de Química Orgánica, Universidad Nacional Autónoma de México, 04510 CDMX, México. E-mail: norberto.farfan@gmail.com
[b] Instituto de Química. Universidad Nacional Autónoma de México, 04510 CDMX, México.
[c] Departamento de Química, Centro de Investigación y de Estudios Avanzados del IPN, México D.F. 07000, A.P. 14-740, México
[d] CNRS, Laboratoire de Chimie de Coordination (LCC), 205 route de Narbonne, BP44099, 31077 Toulouse Cedex 4, France
Electronic Supplementary Information (ESI) available: NMR spectra and computational details. See DOI: 10.1039/x0xx00000x

View Article Online
DOI: 10.1039/D0NJ02576C

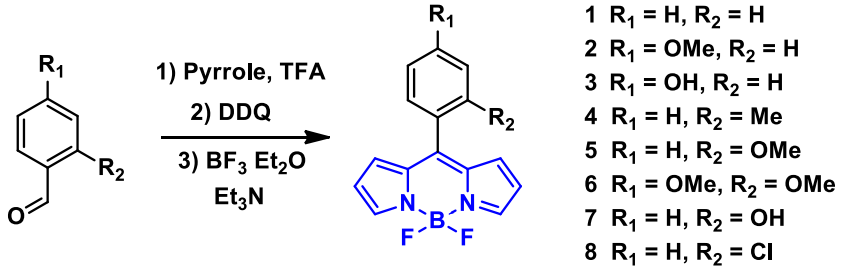

1 R_1 = H, R_2 = H
2 R_1 = OMe, R_2 = H
3 R_1 = OH, R_2 = H
4 R_1 = H, R_2 = Me
5 R_1 = H, R_2 = OMe
6 R_1 = OMe, R_2 = OMe
7 R_1 = H, R_2 = OH
8 R_1 = H, R_2 = Cl
9 R_1 = H, R_2 = F
10 R_1 = H, R_2 = NO_2
11 Pyrenyl

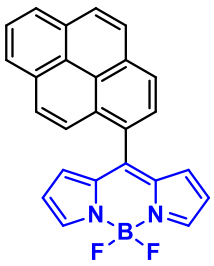

11

Scheme 1. General procedure for synthesis of BODIPY derivatives **1 – 11.**

^{11}B and ^{19}F NMR which provided valuable information concerning the symmetry of the molecule.

Compounds **1-3** showed a typical triplet signal in ^{11}B NMR and a characteristic quartet in ^{19}F NMR due to ^{11}B-^{19}F couplings $^{1}J_{B,F}$ = 28 Hz, which is in accordance with the literature.[19] The ^{19}F NMR spectra for these compounds showed that there is a symmetry plane in the molecule and therefore fluorine atoms are equivalent. The introduction of *ortho* substituents at the phenyl moiety or a bulky group like pyrene restricts the freedom of movement at the *meso* position and therefore the chemical environment for each fluorine atom is different, as evidenced in ^{19}F NMR.

A similar example was reported for a BODIPY having a phenanthrene unit at the *meso*-position.[18] The ^{19}F NMR spectra of BODIPYs **4-11** showed a doublet of quartets for each fluorine atom due to ^{19}F,^{19}F coupling (doublet) and ^{19}F,^{11}B coupling (quartet). As might be expected, the chemical shift difference between the fluorine atoms ($\Delta\delta_F$) varies with the substituent (Fig. 1).

The chemical shift is dependent on the electronical environment that surrounds an atom, thus, the fluorine atom in the opposite side of the *ortho*-substituent is de-shielded and appears to high frequency, while the fluorine atom in the same side as the *ortho*-substituent is shielded and its signal appears to low frequency. The ^{11}B-decoupled ^{19}F NMR spectra denoted as ^{19}F{^{11}B} were also recorded showing a single signal at -145.18 ppm for BODIPY **2** with a -OMe group at the *para* position (Fig. 2a). On the other hand, BODIPY **5** with the -OMe group at the *ortho* position of the phenyl moiety appears as an AB system (Fig. 2b).

The ^{19}F{^{11}B} spectrum of **5** showed a doublet corresponding to one of the fluorine atoms at -144.5 ppm (denoted as F_a) and a doublet for the second fluorine atom (denoted as F_b) at -145.6 ppm with a chemical shift difference of 1.1 ppm and a coupling constant ^{19}F,^{19}F of $^{2}J_{Fa,Fb}$ = 107 Hz.

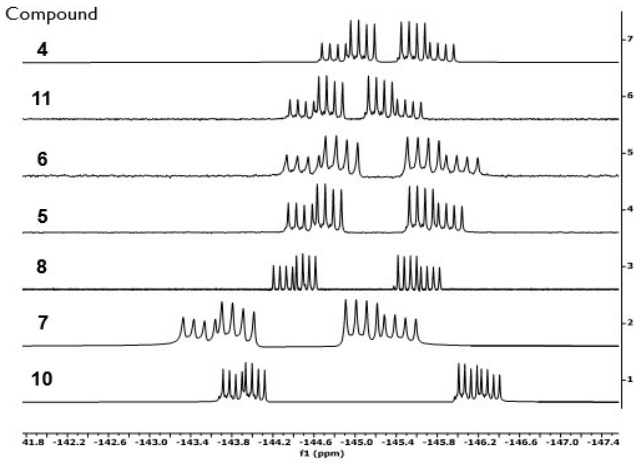

Fig. 1. Stacked ^{19}F NMR spectra of compounds **4-11**. Spectra were stacked from smallest to largest chemical shift difference ($\Delta\delta_F$).

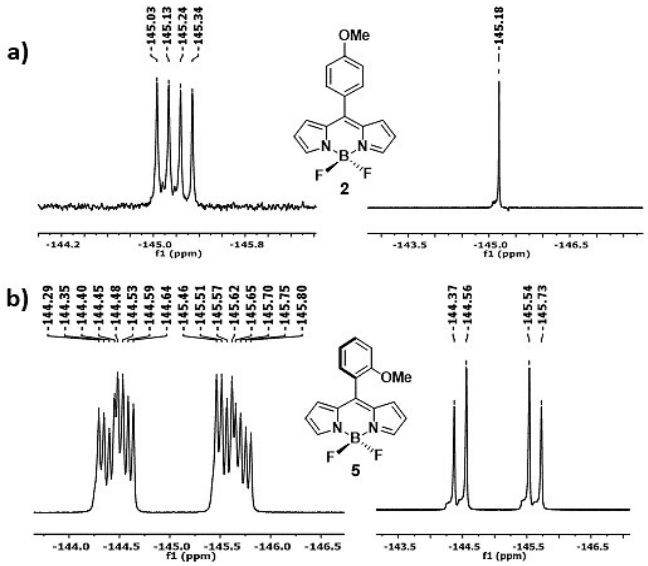

Fig. 2. ^{19}F NMR [564.7 MHz, $CDCl_3$] (left) and ^{19}F{^{11}B} [564.7 MHz, $CDCl_3$] (right) spectra for BODIPY **2** (a) and **5** (b).

View Article Online
DOI: 10.1039/D0NJ02576C

The fact that the rotation of the -OMe substituted phenyl is hindered leads to fluorine atoms that are not equivalent and this kind of compounds can be used to form atropisomers. [20] ^{11}B-decoupled ^{19}F NMR spectra were determined for BODIPYs **4-11** (See supporting information). The obtained chemical shifts and coupling constants of BODIPYs **4-11** are listed in Table 1. Compound **4** with the methyl group in the *ortho* position of the phenyl moiety showed the smallest chemical shift difference ($\Delta\delta_F$ = 0.69 ppm), while BODIPY **10** which has a nitro group showed the largest chemical shift difference ($\Delta\delta_F$ = 2.39 ppm). The ^{19}F NMR spectra in toluene-d_8 (ESI† Fig. S31), determined in the range from 30°C to 90°C, show a 0.6 ppm low-frequency shift but maintained the $\Delta\delta_F$, which means the rotation barrier is > than 16.5 kcal/mol, therefore, rotation over *meso* position does not occur.

Photophysical Properties

Photophysical properties such as absorption maximum ($\lambda_{abs\ max}$), emission maximum ($\lambda_{emis\ max}$), Stokes shift ($\Delta\bar{\upsilon}$) and fluorescence quantum yields (Φ_F) were measured in four different solvents (See Supporting Information, Table S1). The normalized absorption and emission spectra of selected BODIPYs in toluene are shown in Fig. 3.

Regardless of the nature of the *meso*-aryl substituent, the BODIPYs show an origin band around 500 nm that corresponds to $S_0 \rightarrow S_1$ (π-π^*) transition which is slightly redshifted in non-polar solvents such as hexane and toluene. The shoulder at lower wavelength is due to the 0 – 1 vibrational transition. The value of the fluorescence quantum yield is much lower in BODIPYs **1-3** (highest value Φ_F = 0.11 for **2** in toluene) compared to BODIPYs **4–11** (highest value Φ_F = 1.05 for BODIPY **4** in toluene, the value greater than one is relative to the standard Rhodamine 6G). [21] The *ortho* substituents at the phenyl moiety restrict freedom of movement promoting the radiative relaxation pathway. BODIPY **5** with a -OMe group at the *ortho* position has a fluorescence quantum yield four times larger (Φ_F = 0.20) than BODIPY **2** with the -OMe group at the *para* position (Φ_F = 0.05) in hexane. BODIPY **10** with the nitro group showed the smallest values (Φ_F = 0.01 or less) due to their highly efficient intersystem crossing that quenches the fluorescence. [22] The fluorescence spectra are strongly dependent on the polarity of the solvent. Thus, the fluorescence quantum yields are quenched in polar solvents due to electron transfer process. [23]

Table 1. Chemical shifts and coupling constants between ^{19}F and ^{11}B nuclei in $CDCl_3$.

Compound	δ_{Fa}	δ_{Fb}	$\Delta\delta_F$	$J_{Fa,Fb}$ [Hz]	δ_B	$J_{B,F}$ [Hz]
4	-144.87	-145.56	0.69	107	0.31	29
5	-144.47	-145.63	1.16	107	0.30	29
6	-144.56	-145.72	1.16	107	0.29	29
7	-143.72	-144.94	1.22	104	-0.28	28
8	-144.47	-145.67	1.20	107	-0.69	28
9	-143.88	-145.35	1.47	107	-	28
10	-143.92	-146.32	2.39	104	-0.70	28
11	-144.51	-145.26	0.74	104	-0.06	28

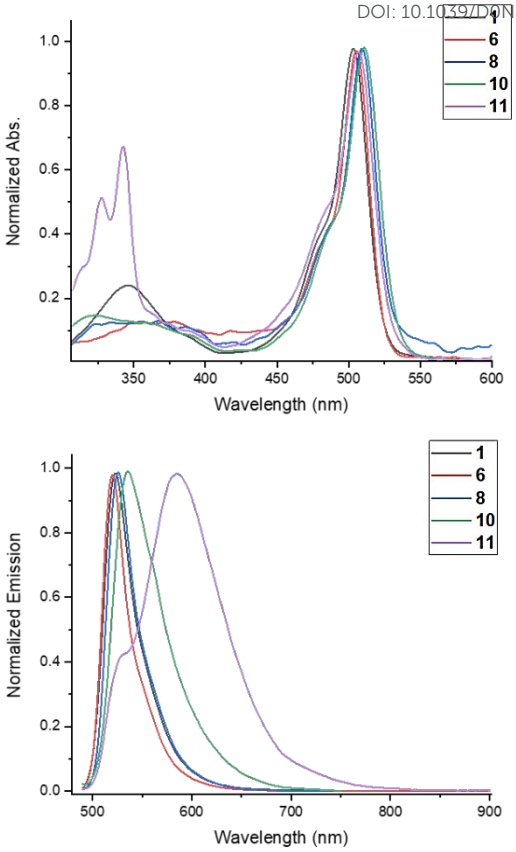

Fig. 3. Normalized absorption and emission spectra of selected BODIPYs **1** (black), **6** (red), **8** (blue), **10** (green) and **11** (purple) in toluene.

The largest Stokes shift is 2688 cm^{-1} for compound **11** in toluene. A plausible explanation for this result is that the maximum emission in toluene for this compound is 587 nm, this red-shifted emission is due to the possible formation of excimers in pyrene. [24] In the absorption spectra, the band in the 300 – 350 nm range shows the characteristic vibronic fine structure of pyrene. [25]

Computational Analysis

Geometry optimizations yielded the global energy minima for the studied BODIPY derivatives, which helped determine that for all the synthesized aryl-substituted compounds, there is a torsion that yields a pronounced dihedral angle between the well-known planar BODIPY moiety and the *o*-aryl plane. Being both planar portions, this characteristic allows to automatically define the dihedral angle.

For the *meso*-phenyl-BODIPY **1** whose substituent would be regarded as the reference for the study, that means hydrogen, such dihedral angle (highlighted cyan atoms in Fig. 4) was calculated as 54.9° and is the smallest among all the *ortho*-substituted systems. The rest of the derivatives show values ranging from 60.6° for fluorine **9** up to 117.7° for the pyrenyl-substituted compound **11**.

View Article Online
DOI: 10.1039/D0NJ02576C

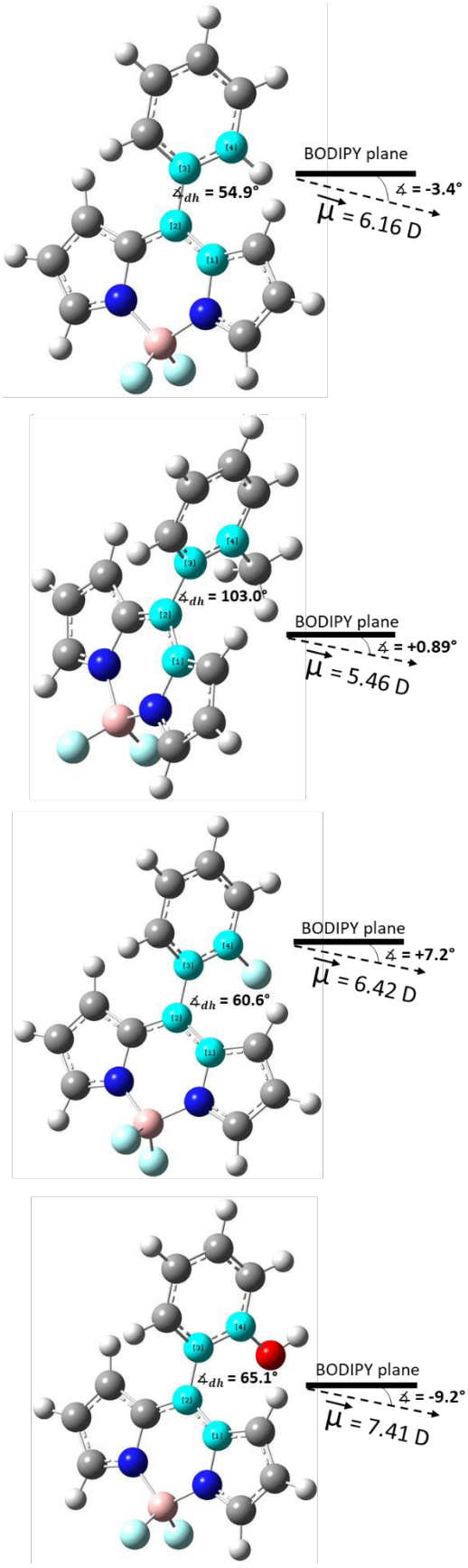

Fig. 4. Dihedral angles and dipole moment vector deviates from the BODIPY plane for compounds **1**, **4**, **7** and **9**.

Fig. 4 gives some examples (compounds **1**, **4**, **7** and **9**) of the calculated structures adding another important feature to the description. The dipole moment vector shows a deviation from the BODIPY plane. This divides the studied species into two sets: the first one includes those derivatives in which the dipole moment vector deviates from the BODIPY plane towards the functional group of interest (H, pyrene, OH and OCH_3 described with a negative angle) and the other set contains those derivatives in which this vector deviates opposite to the location of the highlighted functional group (CH_3, F, Cl and NO_2, described with a positive angle). The remaining compounds can be found within the supporting information (S17-19).

Evaluation of the rotational energy barriers and their influence on the fluorescence quantum yield

Starting from the optimized geometries and the energy minima for *ortho*-substituted species, and the *meso*-(*p*-OMe-phenyl)-BODIPY (**2**) for comparison reasons, the rotational scan provided the torsion angle at which the energy is maximum, and then a transition state TS optimization was carried out to obtain the actual structure for the rotational TS (TS_{rot}) to determine the energy of the rotational barrier for each compound.

The complete series of rotational scans (S20) allowed us to divide the studied species in three groups, one group (compounds **1**, **2**, **5**, **7** and **9**) where the dihedral angle for the ground state (GS) conformation was below 90°. For these species, when the systems reach a dihedral angle of 90° this value corresponds to a local maximum during the scan. These local maxima differ only by 2.5 kcal/mol and, therefore, they could be considered as conformers in equilibrium. The second group (compounds **4**, **10** and **11**) where the GS conformation possesses a dihedral angle larger than 90° and has one true maximum at the TS_{rot}. The final is formed only by the chloride-containing species, whose GS conformation has a dihedral angle in the vicinity of 90°and presents no local minimum.

TS_{rot} structures are shown for selected species in Fig. 5, alongside the rotational barriers for all calculated species, the dihedral angle where the energy maximum is reached, and their corresponding fluorescence quantum yield determined experimentally in this work. The calculated structures evidence that the molecule needs to undergo a deformation from the dipyrromethene plane in order for the *meso* substituent to rotate. All other TS_{rot} geometries can be found in the Supporting Information (S21-24).

A detail not to be disregarded, is that for the *o*-hydroxyl group two conformers were studied, as shown in Fig. 6; one where the OH points towards the BODIPY core and another one pointing away from it. Energy differences for both, the optimized energy minima (1.14 kcal/mol) and their corresponding TS_{rot} (0.97 kcal/mol) were small and, therefore, considered as equilibrium conformers. From these results there are several points to be considered.

View Article Online
DOI: 10.1039/D0NJ02576C

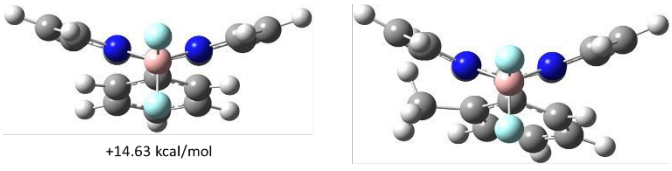

Group	ΔE (kcal/mol)	∢ BODIPY-Ph (°)	Φ_F in hexane
H	+14.63	184.9	0.0300
Pyrene	+28.82	207.7	0.1672
Me	+27.83	193.0	1.0300
F	+18.64	190.6	-
Cl	+27.61	196.8	0.7200
OH	+20.75	190.1	0.3000
o-OMe	+20.00	191.7	0.2000
NO_2	+26.08	199.0	0.0100
p-OMe	+25.10	180.9	0.0500

Fig. 5. Geometries for selected TSrot, rotational barriers and dihedral angles to reach the energy maxima for all computed species and fluorescence quantum yields in hexane.

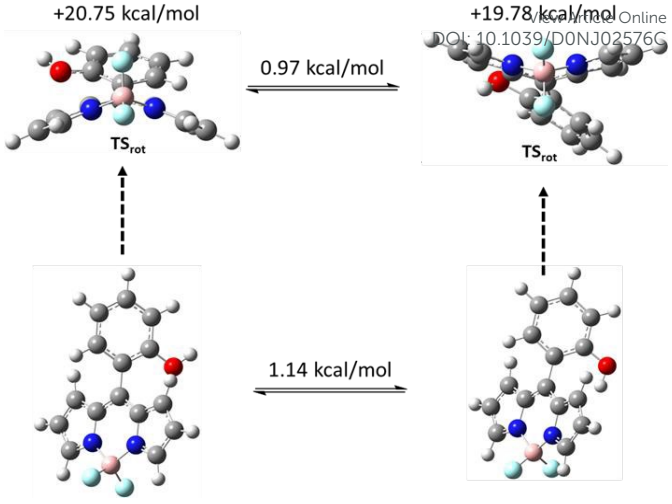

Fig. 6. Calculated hydroxyl-substituted conformers for the study of rotational barriers of compound **7**.

As can be seen in Fig. 5 and 6, the geometry of the dipyrromethene core in the TS_{rot} resembled the nonplanar butterfly shape of what several examples in the literature assign as the geometry for the excited state, S_1.[26–28]

There are two approaches that help explaining the observed Φ_F. The first one is offered by Li and co-workers,[27] and it states that when the chromophore undergoes excitation, the electronic GS reaches a point in the S_1 potential surface that corresponds to a metastable conformation (**M**) of such excited state. From this metastable species the excited chromophore can emit but also relax its structure towards the lowest energy of S_1, that couples with S_0 and then, through internal conversion (IC) passes again to S_0. Therefore, the Φ_F depends on how long the metastable state can endure from appearance to relaxation and IC. For BODIPY **1**, the phenyl torsion in conjunction with the bend dipyrromethene dictate the existence of four isoenergetic conformers, therefore, there are multiple excited state decay pathways. The second approach is offered by Qian and co-workers.[29] Another possibility for the radiative process to be favored is the energy difference for IC. The higher the energy gap for the vertical excitation between the relaxed S_1 conformation to the S_0, TS_{rot}, the longer the IC will last, giving opportunity for emission to occur. It is common that, for these systems, the oscillator strength for the next excited states plays an important role increasing in magnitude, while for S_1 this parameter decreases. According to the cited studies, values over 10 kcal/mol for the IC $S_1 \rightarrow S_0$ allow both emission and IC $S_n \rightarrow S_1$.

As suggested by the trends that were determined computationally, the rotational barriers and the quantum yield are intertwined (in some degree) most likely by the existence of the aforementioned metastable state. BODIPY **1** having the lowest energy barrier also presents the lowest quantum yield.

In contrast, BODIPYs **4** and **8**, having high rotational barriers also present the highest quantum yields, which would lead to assume that the energetic and geometric pathway traversed by the metastable state, allows the involved excited states to relax through emission-favouring pathways.

The two exceptional cases in the studied series are the nitro-substituted BODIPY **10**, because of the highly efficient intersystem crossing,[22] and BODIPY **11** due to the largest number of vibrational modes that pyrene possesses. Nonetheless, despite having those deterring properties, the rotational barrier is high enough to bestow **11** with more than a five-fold increase in quantum yield, compared to **1**.

It is of great importance to mention that the imaginary frequencies for the TS_{rot} are small in magnitude (ranging from -26 cm^{-1} to -73 cm^{-1}) which are not usual for a true TS. This would mean that the photophysical processes for electronic GS or excited states would be more complex that what is intuitive.[26] This complexity calls for more sensitive and more in-depth methodologies that can provide a complete description of dynamics and energetics.

One fact that supports the complexity involved in describing the energetics of these processes is, for example that the barrier for the other computed *p*-substituted compounds (BODIPY **2** and **3** for comparison) shows a decrease in rotational barrier for the *p*-OMe bearing species, but an increase of 66% in quantum yield, which means that for the GS conformation, the rotational process should be even more favored than emission in comparison to the base *meso*-phenyl-BODIPY **1**.

Nonetheless, the electron-donating effect of the *p*-OMe substituent is enough to create some push-pull effect from the methoxy group towards the BODIPY. As an example, if we had an amino group, the electron-donating effect would increase, causing a decrease in the rotational barriers.

View Article Online
DOI: 10.1039/D0NJ02576C

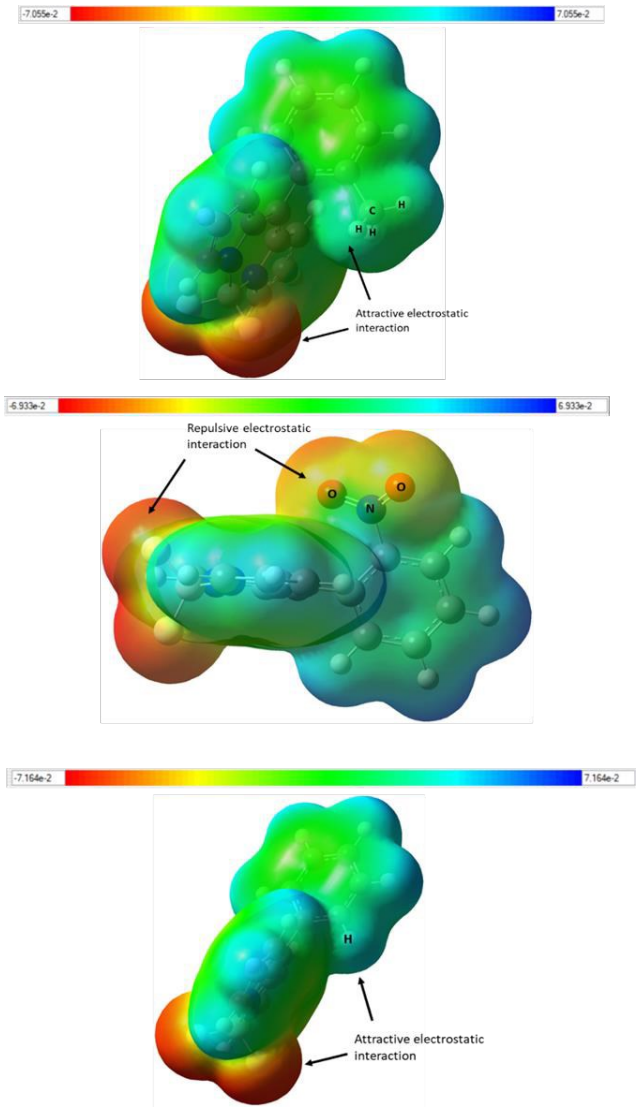

Fig. 7. Electrostatic potential (ESP) maps for some selected species where the difference between attractive and repulsive interactions are observable. Computed with a B3LYP/6-31g(d,p) theory level with a CPCM solvation model in hexane.

This electronic communication can be explained through the *quinoid* canonical form shown in Scheme 2, which, once in the excited state, should adopt a conformation where rotation is precluded in such a way that a radiative relaxation pathway is preferred, increasing the quantum yield with better electron-donating substituents.

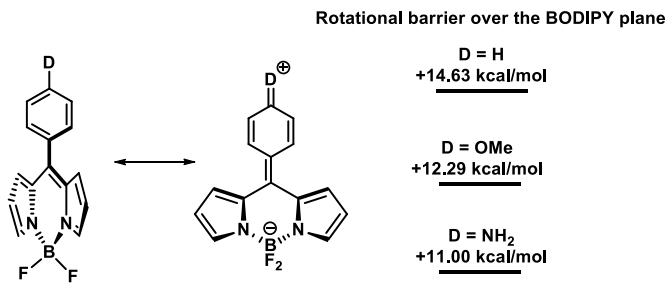

Scheme 2. Quinoid canonical form and the rotational barrier for different donor groups.

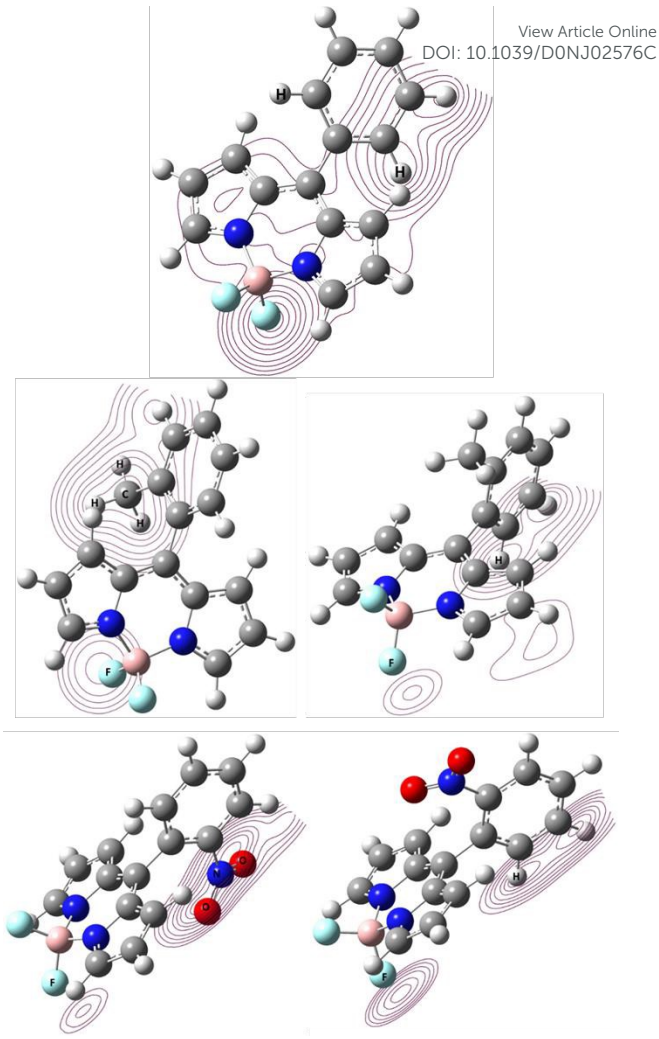

Fig. 8. Level curves for the electrostatic interactions displayed for the plane sectioning the *ortho* substituent. Computed with a B3LYP/6-31g(d,p) theory level with a CPCM solvation model in hexane.

Effect of Electrostatic Features on NMR-Spectroscopic and Photophysical Properties

I. Electrostatic interactions

The computationally obtained structural and physicochemical results show that only the *para*-substituted derivatives (**1-3**) would be energetically allowed to rotate. For the cases in which the *ortho* substituents in the phenyl are energetically locked, an electrostatic and magnetic interaction between the *ortho*-substituents and the nearest fluorine atom gives rise to a difference in chemical shifts ($\Delta\delta_F$), observable in the ^{19}F NMR spectra. Through a series of computational analyses, we were able to find a series of trends that account for the $\Delta\delta_F$.

The first parameter to explore is related to how electrostatic interactions between the fluorine atoms in the BODIPY and the functional group of interest in the phenyl moiety, govern the behavior of $\Delta\delta_F$ which, as can be seen in the ESP maps (obtained at an isovalue of 0.002 in Fig. 7), can vary from attractive (in the case of those BODIPY derivatives with small $\Delta\delta_F$), to repulsive for the species with large difference in chemical shift. This seems to indicate that when the partial charge in the functional

group *ortho* to the BODIPY becomes more negative, the interaction with the closest fluorine atom increases the shielding with respect to their magnetic behavior, increasing the value of $\Delta\delta_F$ as well.

The existence of this electrostatic interaction can be further visualized in the contours calculated at an isovalue of 0.002 presented in Fig. 8. These contours were obtained for the plane crossing the main atom in the functional group of interest. It is observed, for hydrogen, that the plane passing through the center of the atom creates level curves indicative of an interaction with fluorine, and also with the BODIPY fragment. Thus, the other *ortho* hydrogen, is chemically and electrostatically equivalent, this leads to equivalent fluorine atoms and no differences in magnetic behavior. For BODIPY **4** with the methyl group, the carbon and hydrogen atoms are interacting almost solely with fluorine for that level curve and is totally differentiable from the interaction for the remaining *ortho* hydrogen. The fact that there are level curves for the interaction between the methyl and fluorine, and the attractive character of such electrostatic interaction, provides a small but NMR-detectable $\Delta\delta_F$ for the two fluorine atoms. For BODIPY **10** with the nitro substituent, we can observe the particular interaction between the nitro group and the fluorine that produces the $\Delta\delta_F$, and the strongly repulsive character of the interaction yields the largest value among the explored series of BODIPY derivatives. Images for the rest of the studied compounds can be found in the ESI (S25-32).

II. Dipole Moment Vectors and Transition Dipole Moments

Let us revisit the values for the deviation angle between the BODIPY plane and the dipole moment vectors shown in Fig. 4 and make a comparison between the angles, the dipole moments of the studied systems, the transition dipole moments for the main excitation of each one of them and their respective values of fluorescence quantum yield (Φ_F). Calculated dipole moments, the angle regarding the BODIPY plane, and the quantum yield values are given in Table 2.

Setting the fluorescence value of 0.03 for the *meso*-phenyl BODIPY **1** as reference and supported by the rotational barriers studied above, the data shows that, in this case, rotation of the phenyl group is favored over the fluorescence pathway.

As mentioned before, the value for the nitro-containing species decreased threefold, which is typical for nitro-substituted species, since the nitro group quenches fluorescence via intersystem crossing. [22] For all other species, the quantum yield is higher, in accordance with the restricted non-radiative relaxation pathways upon introduction of the *ortho* substituent in the *meso*-phenyl moiety.[26] The Fluorescence quantum yield was plotted as a function of dipole moment vector deviation (S33) and transition dipole moment (Table 2 and Fig. 9). Positive angles in the deviation from the BODIPY plane, correspond to the species with the highest quantum yields, whilst all the negative angles are for species with 0.3 or lower values for this photophysical feature. This creates a valuable design parameter to estimate an interval of quantum yield by calculating the deviation angle thus providing structure-property relationship arguments.

Similarly, three groups can be noticed from the plotted data shown in Fig. 9; the two lowest values (0.01 and 0.03) were explained before, followed by the series of compounds with increased Φ_F (from 0.16 to 0.31) which correspond to those showing hindered rotation and the low values of transition dipole moment. Finally, the last family of compounds, shows a large increase in quantum yield (>0.70) which corresponds to hindered rotation and the largest transition dipole moments, leading to a structure-property relationship argument in terms of the behavior of this electronic characteristic.

III. Group electronegativity and Inductive Effects

Having a series of functional groups that share differently the electron density of the phenyl moiety to which they are bonded, gave us a parameter to be considered. Fig. 10 shows how the $\Delta\delta_F$ changes as the group electronegativity[30] increases for the *ortho* substituents.

Table 2. Selected data of the different groups.

Compound	Group	∢ BODIPY-μ_{calc} (°)[A]	μ_{calc} (D)[A]	S_0 -> S_1 μ_{calc} (D)[B]	Φ_F in hexane[C]
1	**H**	-3.4	6.16	6.66	0.0300
11	**Pyrene**	-8.70	6.40	6.13	0.1672
4	**CH_3**	0.89	5.46	6.87	1.0030
9	**F**	7.2	6.42	6.76	-
8	**Cl**	8.5	6.29	7.00	0.7200
7	**OH**	-9.20	7.41	5.06	0.3100
5	**OCH_3**	-15.7	7.19	6.63	0.2000
10	**NO_2**	-27.4	7.74	6.21	0.0100

[A]Calculated from the geometry optimizations at the B3LYP/def2SVP theory level using the SMD solvation model in hexane.

[B]Calculated through TD-DFT computations at the B3LYP/6-311g(d,p) theory level using the CPCM solvation model in hexane.

[C]Obtained experimentally in this work.

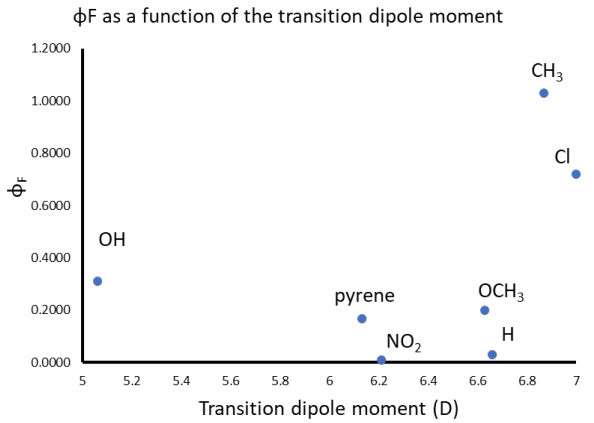

Fig. 9. Fluorescence quantum yield as a function of transition dipole moment.

View Article Online DOI: 10.1039/D0NJ02576C

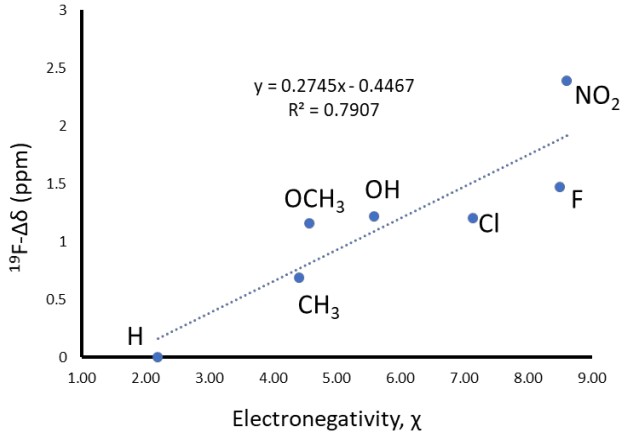

Fig. 10. Δδ as a function of group electronegativity. Group electronegativity values were taken from Ref. (30). $\Delta\delta_F$ values were obtained from the ^{19}F NMR spectra determined in the present contribution.

Plotting the data, a fairly acceptable correlation can be obtained, showing that the variables are directly proportional. The inductive effect is due to differences in electronegativity between atoms bonded together. Based on the relation between electronegativity and the $\Delta\delta_F$, σ-Hammett coefficients related to inductive effects (σi) were also taken into account.[31] Fig. 11 shows that $\Delta\delta_F$ increases as the σ-Hammett coefficients increases.

IV. Functional group hardness/softness

Besides the property of attracting electron density as a functional group, it was important to evaluate the effect of that electron density once distributed in the *ortho* substituent. The hardness/softness of phenyl-substituents was calculated using reported values and equations[32] and the results of the NPA performed, reported as the charge of the ortho functional group (Q_G). That information can be found in Table S2.

With our data treatment we found that monoatomic substituents such as fluoride and chloride are the hardest, followed closely by hydrogen. In the middle of the interval, one finds the hydroxyl and methyl groups.

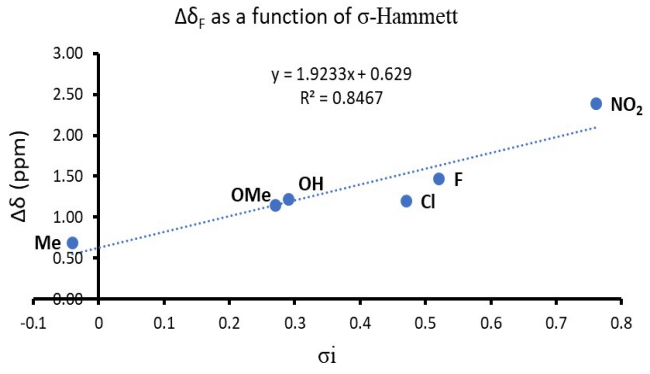

Fig. 11. Linear relationship between $\Delta\delta_F$ and σ_i.

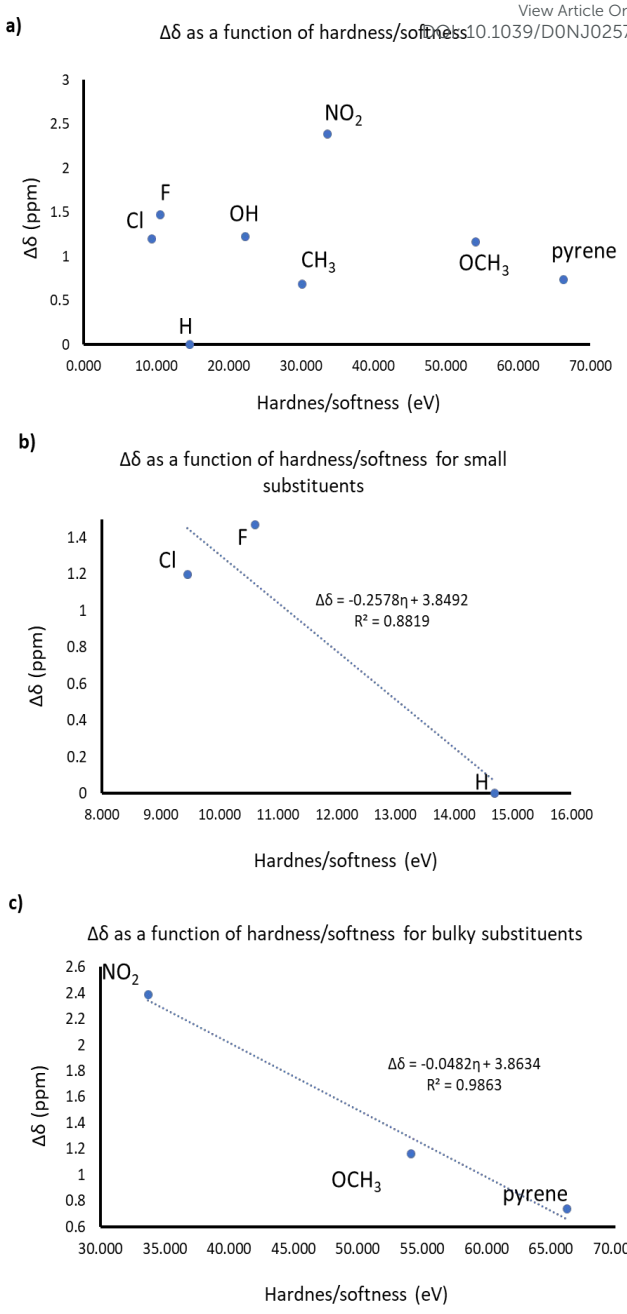

Fig. 12. Plots for the $\Delta\delta_F$ vs hardness/softness data of the studied ortho substituents.

Finally, the nitro group, the methoxy and the pyrenyl are prone to be labelled as soft. It is important to keep in mind that not only the charge located on each functional group is relevant to designate a substituent as soft or hard, but also the thermodynamic properties of ionization potential and electron affinity which are regarded within the Mulliken-Jaffe parameters.

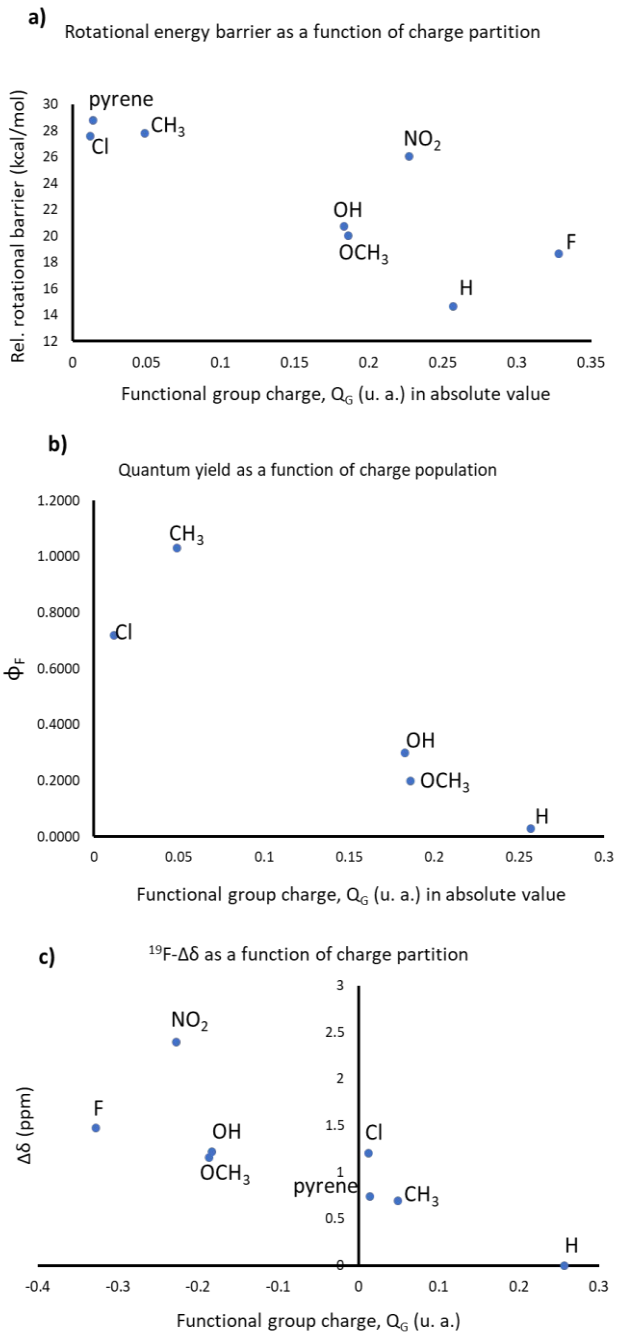

Fig. 13. Trends of rotational energy barrier, fluorescence quantum yield and $\Delta\delta_F$ as a function of the magnitude of the charge partition of the *ortho*-substituent.

Fig. 12 shows the trends found and the correlations between the hardness and softness of the *ortho* substituents and the $\Delta\delta_F$. At first sight, the plotted values show no correlation, however, when the data is divided in sections some information is apparent. For the monoatomic substituents, the hard-functional groups attached to the phenyl moiety, there is a clear correlation between the decreases in $\Delta\delta_F$ as hardness decreases, or as softness increases. The lack of another central point in the data, that may correspond to nitrile, just to provide an example, poses a limitation for claiming a trend or correlation for that section in the plot. In spite of that, there is the third section of the values that also presents a linear, inversely proportional correlation between $\Delta\delta_F$ and softness, which would give different linear behavior depending on the bulkyness of the *ortho* substituent.

Finally, a parameter obtained through NPA charge partition, that brings together all studied and measured features, is the calculated charge for the *ortho*-substituents (Q_G), which establishes a trend with the rotational energy barriers, the $\Delta\delta_F$ and the Φ_F as shown in Fig. 13. For the rotational energy barriers (Fig. 13a) the absolute value of Q_G was used, evidencing a clear trend where the *ortho*-substituents with the largest charge are the ones with a lower rotational barrier, and as the functional group tends to neutrality, the barrier becomes larger. This same trend is observed for Φ_F. Eliminating two cases: nitro derivative **10** due to its low fluorescence for reasons discussed above, and pyrenyl **11** because of the nuances of the exceeding amount of vibrational relaxation modes. Fig 13b shows, that as the absolute value of Q_G becomes larger, the fluorescence quantum yield decreases, meaning that for the substituents close to neutral, we measured the highest values of Φ_F. This would mean that, when the *ortho*-substituent is highly charged, it favors some interactions that help reach the TS_{rot} in non-polar solvents; and, as has already been explained, when the molecule possesses *ortho* hindrance, it favors radiative relaxation. Therefore, large values of Q_G suggest that it is difficult to reach the rotational barrier and how much favored the emission properties would be. Fig. 13c shows the final trend established by Q_G, where it is observed that for positive values of Q_G, $\Delta\delta_F$ decreases. In contrast, the most negatively charged species are the ones with largest $\Delta\delta_F$ values, showing that attractive or repulsive interactions are dictating the magnitude of this magnetic differentiation, as established by the value of Q_G.

Conclusions

A series of *meso*-substituted BODIPYs were synthesized. *Ortho*-aryl substitution proved to be a factor of important influence in the spectroscopic and photophysical properties because of the restriction to phenyl ring rotation. The magnitude and nature of the electrostatic interaction between *ortho*-substituents and the fluorine atoms of the BODIPY gives rise to an observable differentiation by ^{19}F-NMR, which is influenced by group electronegativity, hardness/softness and σ_i-Hammett constant of the *ortho* substituent. As $\Delta\delta_F$ increases, the group electronegativity and the σ-Hammett constants increase.

The *meso*-(*o*-aryl)-BODIPYs, where free rotation of the phenyl group is restricted, leads to an increase in the fluorescence quantum yield compared to the reference *meso*-phenyl-BODIPY in non-polar solvents. Regarding quantum yields, the DFT calculations helped to gain insight into the relevant factors for this photophysical property. In the case of the reference BODIPY and the *p*-substituted analogues, the relaxation interval along the dihedral angle coordinate and the internal conversion $S_1 \rightarrow S_0$ energy are the most important factors that explain the emitting behavior. For the remaining *meso*-(*o*-aryl)-BODIPYs, the relaxation interval for the metastable S_1 conformer is the most important factor to understand the trends in magnitude

View Article Online DOI: 10.1039/D0NJ02576G

for the quantum yield, with some subtle differences between similar substituents for the IC relaxation pathways. Computational studies on the rotational energy barriers and charge partition, provided insight on the TS_{rot} geometries and the close relationship between rotational barriers, $\Delta\delta_F$ and fluorescence quantum yields. The study of these parameters showed a structure-property relationship that provides design arguments for this kind of fluorophores.

Experimental Section

Materials and methods

Chemicals used for the synthesis were reagent grade. Spectroscopic grade solvents were used for all photophysical measurements. ^{1}H, ^{13}C, ^{11}B and ^{19}F NMR spectra were recorded with Bruker 400 MHz, VARIAN Unity Inova 300 MHz and Anasazi 90 MHz spectrometers. Chemical shifts for ^{1}H and ^{13}C NMR spectra are referenced relative to the residual protonated solvent. The ^{11}B NMR chemical shift is referenced relative to $BF_3{\cdot}Et_2O$ (δ = 0 ppm), and the ^{19}F NMR chemical shift is given relative to $CFCl_3$ (δ = 0 ppm). Data are listed in parts per million (ppm). UV-visible spectra were recorded on a VARIAN spectrometer. Fluorescence spectra were recorded on a VARIAN spectrophotometer with a slit width of 10nm, at 480 nm excitation wavelength and emission from 490 to 750 nm. The corresponding fluorescence quantum yield (Φ_f) was calculated according to a standard solution of Rhodamine 6G in ethanol and was determined using the equation below,

$$\Phi_x = \Phi_s \left(\frac{A_s}{A_x}\right)\left(\frac{F_x}{F_s}\right)\left(\frac{n_x}{n_s}\right)^2$$

Where Φ is the fluorescence quantum yield, A is the absorbance, F corresponds to the area under the emission curve and n is the refractive index of the solvents used in the measurement. The subscripts x and s represent the tested dye and the standard dye (Rhodamine), respectively.

General Synthesis

Synthesis of dipyrromethanes: To a solution of the corresponding aromatic aldehyde (1 eq) in pyrrole (4 eq), was added a catalytic amount of trifluoroacetic acid (TFA). The mixture was stirred at room temperature until total consumption of the aldehyde. The crude product was washed with brine, extracted with CH_2Cl_2, dried over anhydrous Na_2SO_4 and evaporated to dryness under vacuum. This crude was then purified in column chromatography on silica gel using hexane/ethyl acetate.[33]

Synthesis of BODIPYs: Into the corresponding dipyrromethane dissolved in CH_2Cl_2, DDQ (1 eq) was added and the solution was stirred 1 h at room temperature. To this oxidized product, $BF_3{\cdot}Et_2O$ (6 eq) was added under nitrogen atmosphere and stirred for another 15 min, then, triethylamine (3 eq) was added dropwise and stirring was continued to completion of the reaction which was monitored by TLC. The reaction mixture was then washed with brine and extracted with CH_2Cl_2, the organic layer was combined, dried over Na_2SO_4 and evaporated to dryness under vacuum to give the crude product. This was further purified by silica gel column chromatography to afford the corresponding BODIPY.[34]

Characterization

4,4-difluoro-8-phenyl-4-bora-3a,4a-diaza-s-indacene (**1**). Column chromatography using hexane/ethyl acetate (8:2) afforded **1**[26] as a green crystalline solid (60%). Mp: 103 °C. ^{1}H NMR [400 MHz, $CDCl_3$] (δ, ppm): 7.95 (m, 2H), 7.51–7.60 (m, 5H), 6.94 (d, *J* = 3.6 Hz, 2H), 6.55 (d, *J* = 3.6 Hz, 2H); ^{13}C NMR [100 MHz, $CDCl_3$] (δ, ppm): 147.3, 144.0, 134.9, 133.7, 131.6, 130.74, 130.44, 128.4. ^{11}B NMR [160 MHz, $CDCl_3$] (δ, ppm): -0.29 (t, $J_{B\text{-}F}$ = 29 Hz). ^{19}F NMR [282 MHz, $CDCl_3$] (δ, ppm): -144.98 (q, $J_{B\text{-}F}$ = 29 Hz).

4,4-difluoro-8-(4-methoxyphenyl)-4-bora-3a,4a-diaza-s-indacene (**2**)**.** Column chromatography with hexane/ethyl acetate (8:2) afforded **2**[35] as an orange powder (61%). Mp: 120–122 °C. ^{1}H NMR [400 MHz, $CDCl_3$] (δ, ppm): 7.92 (s, 2H), 7.55 (d, *J* = 8.8 Hz, 2H), 7.05 (d, *J* = 8.9 Hz, 2H), 6.98 (d, *J* = 4 Hz, 2H), 6.56 – 6.54 (m, 2H), 3.92 (s, 3H). ^{13}C NMR [100 MHz, $CDCl_3$] (δ, ppm): 162.3, 147.7, 143.6, 135.1, 132.6, 131.6, 126.6, 118.4, 114.3, 55.7. ^{11}B NMR [160 MHz, $CDCl_3$] (δ, ppm): -0.26 (t, $J_{B\text{-}F}$ = 28 Hz). ^{19}F NMR [282 MHz, $CDCl_3$] (δ, ppm): -145.19 (q, $J_{B\text{-}F}$ = 28 Hz).

4,4-difluoro-8-(4-hydroxyphenyl)-4-bora-3a,4a-diaza-s-indacene (**3**)**.** Column chromatography using hexane/ethyl acetate (8:2) afforded **3**[36] as a red crystalline solid (46%). Mp: 151 °C. ^{1}H NMR [400 MHz, $CDCl_3$] (δ, ppm): 7.95 (s, 2H), 7.50 (d, *J* = 8.6 Hz, 2H), 6.99 (m, 4H), 6.57 (d, *J* = 2.4 Hz, 2H), 5.82 (s, 1H). ^{13}C NMR [100 MHz, $CDCl_3$] (δ, ppm): 158.6, 147.4, 143.5, 134.8, 132.6, 131.4, 126.3, 118.4, 115.6. ^{11}B NMR [160 MHz, $CDCl_3$] (δ, ppm): -0.25 (t, $J_{B\text{-}F}$ = 28 Hz). ^{19}F NMR [376 MHz, $CDCl_3$] (δ, ppm): -144.56 (q, $J_{F\text{-}B}$ = 29 Hz).

4,4-difluoro-8-(2-methylphenyl)-4-bora-3a,4a-diaza-s-indacene (**4**)**.** Column chromatography using hexane/ethyl acetate (8:2) afforded **4**[26] as a green solid (10%). Mp: 135 °C. ^{1}H NMR [400 MHz, $CDCl_3$] (δ, ppm): 7.93 (s, 2H), 7.45 – 7.39 (m, 1H), 7.33 (d, *J* = 7.9 Hz, 1H), 7.30 – 7.23 (m, 2H), 6.71 (d, *J* = 4.1 Hz, 2H), 6.49 (d, *J* = 4.0 Hz, 2H), 2.24 (s, 3H). ^{13}C NMR [100 MHz, $CDCl_3$] (δ, ppm): 147.2, 144.5, 136.5, 135.6, 133.1, 131.2, 130.6, 129.9, 129.8, 125.4, 118.7, 20.1. ^{11}B NMR [128 MHz, $CDCl_3$] (δ, ppm): 0.31 (t, $J_{B\text{-}F}$ = 28 Hz). ^{19}F NMR [376 MHz, $CDCl_3$] (δ, ppm): -144.87 (dq, $J_{B\text{-}Fa}$ = 28 Hz, $J_{F\text{-}F}$ = 104 Hz), - 145.56 (dq, $J_{B\text{-}Fb}$ = 28 Hz, $J_{F\text{-}F}$ = 104 Hz).

4,4-difluoro-8-(2-methoxyphenyl)-4-bora-3a,4a-diaza-s-indacene (**5**)**.** Column chromatography using hexane/ethyl acetate (8:2) afforded **5**[37] as an orange powder (20%). Mp: 110 – 112 °C. ^{1}H NMR [400 MHz, $CDCl_3$] (δ, ppm): 7.90 (s, 2H), 7.50

View Article Online
DOI: 10.1039/D0NJ02575D

(td, J = 8.3 Hz, J = 1.6 Hz, 1H), 7.31 (dd, J = 7.5 Hz, J = 1.6 Hz, 1H), 7.08–7.03 (m, 2H), 6.80 (d, J = 4.0 Hz, 2H), 6.48 (d, J = 4.0 Hz, 2H), 3.75 (s, 3H). ^{13}C NMR [100 MHz, CDCl3] (δ, ppm): 157.2, 144.5, 143.8, 135.7, 131.6, 131.5, 131.1, 122.4, 120.1, 118.1, 111.3, 55.6. ^{11}B NMR [128 MHz, $CDCl_3$] (δ, ppm): 0.31 (t, J_{B-F} = 28 Hz). ^{19}F NMR [376 MHz, $CDCl_3$] (δ, ppm): -144.47 (dq, J_{B-Fa} = 28 Hz, J_{F-F} = 104 Hz), -145.63 (dq, J_{B-Fb} = 28 Hz, J_{F-F} = 104 Hz).

4,4-difluoro-8-(2,4-dimethoxyphenyl)-4-bora-3a,4a-diaza-s-indacene (**6**)**.** Column chromatography using hexane/ethyl acetate (8:2) afforded **6** as a red powder (25%). Mp: 156–157 °C. FTIR-ATR (υ, cm^{-1}): 3108, 2937, 1383, 1255, 1167, 1110, 1063, 979, 837, 780, 746, 706, 618, 582, 420. ^{1}H NMR [400 MHz, $CDCl_3$] (δ, ppm): 7.87 (s, 2H), 7.24 (d, *J* = 9 Hz, 1H), 6.83 (d, J = 3.6 Hz, 2H), 6.59 (d, *J* = 6.4 Hz, 2H), 6.47 (d, *J* = 3.6 Hz, 2H), 3.89 (s, 3H), 3.73 (s, 3H). ^{13}C NMR [100 MHz, $CDCl_3$] (δ, ppm): 162.7, 158.7, 144.6, 144.3, 136.4, 132.9, 131.5, 117.9, 115.3, 104.3, 99.0, 55.6, 55.5. ^{11}B NMR [128 MHz, $CDCl_3$] (δ, ppm): 0.29 (t, J_{B-F} = 29 Hz). ^{19}F NMR [282 MHz, $CDCl_3$] (δ, ppm): −144.56 (dq, J_{B-Fa} = 29 Hz, J_{F-F} = 107 Hz), −145.72 (dq, J_{B-Fb} = 29 Hz, J_{F-F} = 107 Hz). HRMS-ESI-TOF: Experimental mass for $C_{17}H_{15}BFN_2O_2$ *m/z* 309.120512; calculated *m/z* 309.1211 for $C_{17}H_{15}BFN_2O_2$; % error: 0.361884; $[M-F]^+$

4,4-difluoro-8-(2-hydroxyphenyl)-4-bora-3a,4a-diaza-s-indacene (**7**)**.** Column chromatography using hexane/ethyl acetate (8:2) afforded **7**[38] as a green powder (10%). Mp: 134–136 °C. ^{1}H NMR [300 MHz, $CDCl_3$] (δ, ppm): 7.89 (s, 2H), 7.4 (td, J = 7.2 Hz, J = 1.7 Hz, 1H) 7.25 (dd, J = 7.7 Hz, J_2 = 1.7 Hz, 1H), 7.04 – 6.89 (m, 2H), 6.90 (d, J = 3.6 Hz, 2H), 6.49 (d, J = 3.9 Hz, 2H). ^{13}C NMR [75 MHz, $CDCl_3$] (δ, ppm): 153.6, 144.8, 143.0, 135.2, 132.1, 131.6, 120.4, 120.1, 120.0, 119.0, 117.1. ^{11}B NMR [160 MHz, $CDCl_3$] (δ, ppm): -0.28 (t, J_{B-F} = 28 Hz). ^{19}F NMR [282 MHz, $CDCl_3$] (δ, ppm): −143.72 (dq, J_{B-Fa} = 28 Hz, J_{F-F} = 104 Hz), −144.94 (dq, J_{B-Fb} = 28 Hz, J_{F-F} = 104 Hz).

4,4-difluoro-8-(2-chlorophenyl)-4-bora-3a,4a-diaza-s-indacene (**8**)**.** Column chromatography using hexane/acetone (9:1) afforded **8** as an orange-green crystalline solid (23%). Mp: 103 °C. ^{1}H NMR [400 MHz, $CDCl_3$] (δ, ppm): 7.94 (s, 2H), 7.58 – 7.52 (m, 1H), 7.52 – 7.45 (m, 1H), 7.43 – 7.35 (m, 2H), 6.73 (d, *J* = 4.1 Hz, 2H), 6.51 (d, *J* = 4.1 Hz, 2H). ^{13}C NMR [100 MHz, $CDCl_3$] (δ, ppm): 145.1, 143.5, 135.4, 133.3, 132.5, 131.6, 131.2, 131.2, 130.3, 126.6, 118.9. ^{11}B NMR [128 MHz, $CDCl_3$] δ -0.68 (t, *J* = 28 Hz). ^{19}F [376 MHz, $CDCl_3$] δ -144.47 (dq, J_{B-Fa} = 28 Hz, J_{F-F} = 105 Hz), - 145.67 (dq, J_{B-Fb} = 28 Hz, J_{F-F} = 105 Hz). ES-MS: ($C_{15}H_{10}BClF_2N_2$) 283.5 $[M^+ - F]$.

4,4-difluoro-8-(2-fluorophenyl)-4-bora-3a,4a-diaza-s-indacene (**9**)**.** Column chromatography using hexane/ethyl acetate (9:1) afforded **9** as a red crystalline solid (16%). ^{1}H NMR [90 MHz, $CDCl_3$] (δ, ppm): 7.49 (s, 2H), 7.24 – 6.77 (m, 4H), 6.51 (d, *J* = 3.8 Hz, 2H), 6.18 (d, *J* = 4.0 Hz, 2H). ^{19}F NMR [84.7 MHz, $CDCl_3$] δ -110.86 (s), -143.88 (dq, J_{B-Fa} = 28 Hz, J_{F-F} = 104 Hz), - 145.35 (dq, J_{B-Fb} = 28 Hz, J_{F-F} = 104 Hz).

4,4-difluoro-8-(2-nitrophenyl)-4-bora-3a,4a-diaza-s-indacene (**10**)**.** Column chromatography using hexane/ethyl acetate (8:2) afforded **10**[20] as an orange solid (14%). Mp: 198 °C ^{1}H NMR [500 MHz, $CDCl_3$] (δ, ppm): 8.22 (dd, *J* = 7.8, 1.6 Hz, 1H), 7.95 (s, 2H), 7.84 – 7.69 (m, 2H), 7.57 (dd, *J* = 7.4, 1.6 Hz, 1H), 6.67 (d, *J* = 4.2 Hz, 2H), 6.51 (d, *J* = 4.3 Hz, 2H). ^{13}C NMR [125 MHz, $CDCl_3$] (δ, ppm): 149.1, 145.3, 142.6, 134.6, 133.2, 132.3, 131.3, 129.8, 128.4, 125.2, 119.2. ^{11}B NMR [160 MHz, $CDCl_3$] δ -0.69 (t, *J* = 28 Hz). ^{19}F [470 MHz, $CDCl_3$] δ -143.92 (dq, J_{B-Fa} = 28 Hz, J_{F-F} = 104 Hz), - 146.32 (dq, J_{B-Fb} = 28 Hz, J_{F-F} = 104 Hz).

4,4-difluoro-8-(1-pyrenyl)-4-bora-3a,4a-diaza-s-indacene (**11**)**.** Column chromatography using hexane/ethyl acetate (9:1) afforded **11**[17] as a green crystalline powder (20% yield). Mp: 134−135 °C. ^{1}H NMR [400 MHz, $CDCl_3$] (δ, ppm): 8.3 – 8.0 (m, 11H), 6.62 (d, *J* = 4.2 Hz, 2H), 6.46 (d, *J* = 3.0 Hz, 2H). ^{13}C NMR [100 MHz, $CDCl_3$] (δ, ppm): 146.6, 144.5, 136.6, 132.6, 131.8, 131.4, 130.8, 130.5, 129.1, 128.6, 127.9, 127.9, 127.2, 126.7, 126.3, 126.0, 125.0, 124.6, 124.3, 124.1, 118.9 ^{11}B NMR [160 MHz, $CDCl_3$] (δ, ppm): -0.06 (t, J_{B-F} = 28 Hz). ^{19}F NMR [282 MHz, $CDCl_3$] (δ, ppm): −144.51 (dq, J_{B-Fa} = 28 Hz, J_{F-F} = 104 Hz), −145.26 (dq, J_{B-Fb} = 28 Hz, J_{F-F} = 104 Hz).

Computational Methodology

All calculations were carried out taking hexane as solvent, trying to match or correlate experimental observations in a solvent with good emission properties and discarding toluene to avoid possible π-stacking interactions with the studied species.

Geometry optimizations were carried out through all-electron calculations using the B3LYP hybrid functional at the def2SVP theory level using the SMD solvation approach, to obtain the geometries of lowest energy for the studied species and to analyze important structural details. Regarding the computation of rotational barriers, all geometries were re-optimized with the M06-2X hybrid functional and the def2SVP basis set using the SMD solvation model to refine the computation of energetics. Scans through redundant coordinates for the dihedral angle between the BODIPY and the *meso* substituents were done using M06-2X/def2SVP approach with the SMD solvation model. Being this combination a proven approach in the field of thermochemistry, energetics, energy barriers, among other features.[39–41]

The energy maximum of each corresponding scan was then optimized as a transition state (TS) to determine the real geometry and rotational barrier of such TSs. This was done also with the M06-2X/def2SVP theory level and SMD solvation approach. Time-dependent Density Functional Theory (TD-DFT) calculations were run using the same functional at the 6-311g(d,p) theory level with the CPCM solvation method, to obtain the value for the dipole moment corresponding to the main transition ($S_0 \rightarrow S_1$) for all BODIPY derivatives.

After determining the orbital behavior of the $S_0 \rightarrow S_1$ transition, the energetic evolution of S_1 was calculated at the M06-2X/def2SVP theory level using the SMD solvation method in hexane, by TDDFT approach to the most representative points

in the rotational scan. The vertical transition energies would shape the curve for the energy of the S_1 excited state for each species, as a function of dihedral angle, to be compared with the rotational energy barriers, this is an approach known in the literature to describe similar phenomena to the one studied in our contribution.[42] The same analysis was carried out for S_2 and S_3 excited states and the respective oscillator strengths for the three excited states.

Natural Population Analysis (NPA) was performed for all compounds using the B3LYP functional at the 6-31g(d,p) theory level to calculate the charge partition for all atoms in the studied species and thus, calculate hardness/softness of the functional groups in the aryl portions of the BODIPY derivatives. Electrostatic potential (ESP) maps as surfaces and contours were produced to analyze the distribution of electrostatic partition in all the studied molecules, these computations were done using the CPCM solvation model.

All calculations were run using the Gaussian 09 software and the GaussView 5.0 visualization suite.[43]

Conflicts of interest

There are no conflicts to declare.

Acknowledgements

MFP (576515) and OGA (239984) thank CONACYT for their doctoral scholarship. The authors acknowledge financial support from CONACYT, PAIP and PAPIIP IN222819 and the French-Mexican International Laboratory (LIA-LCMMC-CONACYT). Thanks to María Luisa Rodríguez, María Eugenia Ochoa for NMR experiments and Geiser Cuellar for Mass Spectra.

Notes and References

(1) Treibs, A.; Kreuzer, F.-H. *Justus Liebigs Ann. Chem.* **1968**, *718*, 208–223.

(2) Lakshmi, V.; Lee, W.-Z.; Ravikanth, M. *Dalt. Trans.* **2014**, *43*, 16006–16014.

(3) Loudet, A.; Burgess, K. *Chem. Rev.* **2007**, *107*, 4891–4932.

(4) Kálai, T.; Hideg, K. *Tetrahedron* **2006**, *62*, 10352–10360.

(5) Choi, S.; Bouffard, J.; Kim, Y. *Chem. Sci.* **2014**, *5*, 751–755.

(6) Guo, H.; Jing, Y.; Yuan, X.; Ji, S.; Zhao, J.; Li, X.; Kan, Y. *Org. Biomol. Chem.* **2011**, *9*, 3844–3853.

(7) Bura, T.; Retailleau, P.; Ulrich, G.; Ziessel, R. *J. Org. Chem.* **2011**, *76*, 1109–1117.

(8) Xochitiotzi-Flores, E.; Islas-Mejía, A. A.; García-Ortega, H.; Romero-Ávila, M.; Mendez-Stivalet, J. M.; Carreón-Castro, M. D. P.; Santillan, R.; Maldonado-Domínguez, M.; Arcos-Ramos, R.; Farfán, N. *J. Organomet. Chem.* **2016**, *805*, 148–157.

(9) Singh, S. P.; Gayathri, T. *European J. Org. Chem.* **2014**, *2014*, 4689–4707.

(10) Ozdemir, M.; Choi, D.; Kwon, G.; Zorlu, Y.; Cosut, B.; Kim, H.; Facchetti, A.; Kim, C.; Usta, H. *ACS Appl. Mater. Interfaces* **2016**, *8*, 14077–14087.

(11) Dale, C. L.; Hill, S. J.; Kellam, B. *Med. Chem. Commun.* **2012**, *3*, 333–338.

(12) Xochitiotzi-Flores, E.; Jiménez-Sánchez, A.; García-Ortega, H.; Sánchez-Puig, N.; Romero-Ávila, M.; Santillan, R.; Farfán, N. *New J. Chem.* **2016**, *40*, 4500–4512.

(13) Awuah, S. G.; You, Y. *RSC Adv.* **2012**, *2*, 11169.

(14) Ziessel, R.; Ulrich, G.; Harriman, A. *New J. Chem.* **2007**, *31*, 496–501.

(15) Tram, K.; Yan, H.; Jenkins, H. a.; Vassiliev, S.; Bruce, D. *Dye. Pigment.* **2009**, *82*, 392–395.

(16) Merkushev, D. A.; Usoltsev, S. D.; Marfin, Y. S.; Pushkarev, A. P.; Volyniuk, D.; Grazulevicius, J. V.; Rumyantsev, E. V. *Mater. Chem. Phys.* **2017**, *187*, 104–111.

(17) Bañuelos, J.; Arroyo-Córdoba, I. J.; Valois-Escamilla, I.; Alvarez-Hernández, A.; Peña-Cabrera, E.; Hu, R.; Zhong Tang, B.; Esnal, I.; Martínez, V.; López Arbeloa, I. *RSC Adv.* **2011**, *1*, 677–684.

(18) Benniston, A. C.; Harriman, A.; Whittle, V. L.; Zelzer, M. *European J. Org. Chem.* **2010**, 523–530.

(19) Hermanek, S. *Chem. Rev.* **1992**, *92*, 352–362.

(20) Doulain, P.-E.; Goze, C.; Bodio, E.; Richard, P.; Decréau, R. A. *Chem. Commun. (Camb).* **2016**, *52*, 4474–4477.

(21) Kubin, R. F.; Fletcher, A. N. *J. Lumin.* **1982**.

(22) Collado-Fregoso, E.; Zugazagoitia, J. S.; Plaza-Medina, E. F.; Peon, J. *J. Phys. Chem. A* **2009**, *113*, 13498–13508.

(23) Ulrich, G.; Ziessel, R.; Harriman, A. *Angew. Chem. Int. Ed. Engl.* **2008**, *47*, 1184–1201.

(24) Winnik, F. *Chem. Rev.* **1993**, *93*, 587–614.

(25) Niko, Y.; Sasaki, S.; Narushima, K.; Sharma, D. K.; Vacha, M.; Konishi, G. I. *J. Org. Chem.* **2015**, *80*, 10794–10805.

(26) Kee, H. L.; Kirmaier, C.; Yu, L.; Thamyongkit, P.; Youngblood, W. J.; Calder, M. E.; Ramos, L.; Noll, B. C.; Bocian, D. F.; Scheidt, W. R.; Birge, R. R.; Lindsey, J. S.; Holten, D. *J. Phys. Chem. B* **2005**, *109*, 20433–20443.

(27) Li, F.; Yang, S. I.; Ciringh, Y.; Seth, J.; Martin, C. H.; Singh, D. L.; Kim, D.; Birge, R. R.; Bocian, D. F.; Holten, D.; Lindsey, J. S.; Carolina, N.; V, W. U.; Louis, S. *J. Am. Chem. Soc.* **1998**, *120*, 10001–10017.

(28) Jiao, L.; Yu, C.; Wang, J.; Briggs, E. A.; Besley, N. A.; Robinson, D.; Ruedas-Rama, M. J.; Orte, A.; Crovetto, L.; Talavera, E. M.; Alvarez-Pez, J. M.; Van Der Auweraer, M.; Boens, N. *RSC Adv.* **2015**, *5*, 89375–89388.

(29) Qian, H.; Cousins, M. E.; Horak, E. H.; Wakefield, A.; Liptak, M. D.; Aprahamian, I. *Nat. Chem.* **2017**, *9*, 83–87.

(30) De Proft, F.; Langenaeker, W.; Geerlings, P. *J. Phys. Chem.* **1993**, *97*, 1826–1831.

(31) Takahata, Y.; Chong, D. P. *Int. J. Quantum Chem.* **2005**, *103*, 509–515.

(32) Kaya, S.; Kaya, C. *Mol. Phys.* **2015**, *113*, 1311–1319.

(33) Gryko, D. T.; Gryko, D.; Lee, C.-H. *Chem. Soc. Rev.* **2012**, *41*, 3780–3789.

(34) Wagner, R. W.; Lindsey, J. S. *Pure Appl. Chem.* **1996**, *68*, 1373–1380.

(35) Betancourt-Mendiola, L.; Valois-Escamilla, I.; Arbeloa, T.; Bañuelos, J.; López Arbeloa, I.; Flores-Rizo, J. O.; Hu, R.;

View Article Online
DOI: 10.1039/D0NJ02576C

Lager, E.; Gómez-Durán, C. F. A.; Belmonte-Vázquez, J. L.; Martínez-González, M. R.; Arroyo, I. J.; Osorio-Martínez, C. A.; Alvarado-Martínez, E.; Urías-Benavides, A.; Gutiérrez-Ramos, B. D.; Tang, B. Z.; Peña-Cabrera, E. *J. Org. Chem.* **2015**, *80*, 5771–5782.

(36) Baruah, M.; Qin, W.; Basarić, N.; De Borggraeve, W. M.; Boens, N. *J. Org. Chem.* **2005**, *70*, 4152–4157.

(37) Roacho, R. I.; Metta-Magaña, A. J.; Peña-Cabrera, E.; Pannell, K. H. *J. Phys. Org. Chem.* **2013**, *26*, 345–351.

(38) Kim, T.-I.; Maity, S. B.; Bouffard, J.; Kim, Y. *Anal. Chem.* **2016**, *88*, 9259–9263.

(39) Mardirossian, N.; Head-Gordon, M. *J. Chem. Theory Comput.* **2016**, *12*, 4303–4325.

(40) Weigend, F.; Ahlrichs, R. *Phys. Chem. Chem. Phys.* **2005**, *7*, 3297–3305.

(41) Marenich, A. V.; Cramer, C. J.; Truhlar, D. G. *J. Phys. Chem. B* **2009**, *113*, 6378–6396.

(42) Kubli-Garfias, C.; Salazar-Salinas, K.; Perez-Angel, E. C.; Seminario, J. M. *J. Mol. Model.* **2011**, *17*, 2539–2547.

(43) Frisch, M. J.; Trucks, G. W.; Schlegel, H. B.; Scuseria, G. E.; Robb, M. A.; Cheeseman, J. R.; Sacalmani, G.; Barone, V.; Menucci, B.; Petersson, G. A.; Nakatsuji, H.; Caricato, M.; Li, X.; Hratchian, H. P.; Izmaylov, A. F.; Bloino, J.; Zheng, G.; Sonnenberg, J. L.; Hada, M.; Ehara, M.; Toyota, K.; Fukuda, R.; Hasegawa, J.; Ishida, M.; Nakajima, T.; Honda, Y.; Kitao, O.; Nakai, H.; Vreven, T.; Montgomery, J. A.; Peralta, J. E.; Ogliaro, F.; Bearpak, M.; Heyd, J. J.; Brothers, E.; Kudin, K. N.; Staroverov, V. N.; Kobayashi, R.; Normand, J.; Raghavachari, K.; Rendell, A.; Burant, J. C.; Iyengar, S. S.; Tomasi, J.; Cossi, M.; Rega, N.; Millam, J. M.; Klene, M.; Knox, J. E.; Cross, J. B.; Bakken, V.; Adamo, C.; Jaramillo, J.; Gomperts, R.; Stratmann, R. E.; Yazyev, O.; Austin, A. J.; Cammi, R.; Pomelliv, C.; Ochterski, J. W.; Martin, R. L.; Morokuma, K.; Zakrzewsli, V. G.; Voth, G. A.; Salvador, P.; Dannenberg, J. J.; Dapprich, S.; Daniels, A. D.; Farkas, O.; Foresman, J. B.; Ortiz, J. V.; Ciolowski, J.; Fox, J. Gaussian 09, Revisions, A.02, Revision D.01, Gaussian, Inc., Wallingfrod, CT, 2009.

View Article Online
DOI: 10.1039/D0NJ02576C

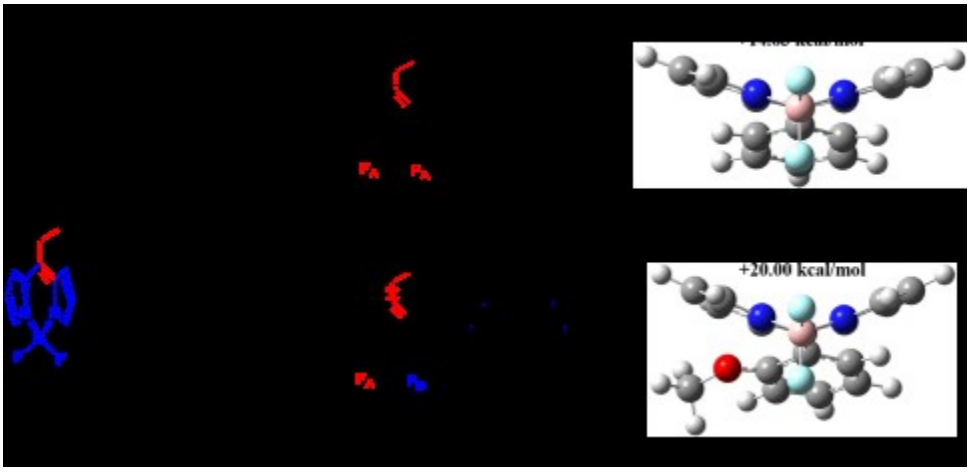

81x39mm (150 x 150 DPI)